Article

Ice retreat in Wilkes Basin of East Antarctica during a warm interglacial

https://doi.org/10.1038/s41586-020-2484-5

Received: 19 November 2019

Accepted: 21 May 2020

Published online: 22 July 2020

Check for updates

T. Blackburn[1]✉, G. H. Edwards[1], S. Tulaczyk[1], M. Scudder[1], G. Piccione[1], B. Hallet[2], N. McLean[3], J. C. Zachos[1], B. Cheney[1] & J. T. Babbe[1]

Efforts to improve sea level forecasting on a warming planet have focused on determining the temperature, sea level and extent of polar ice sheets during Earth's past interglacial warm periods[1–3]. About 400,000 years ago, during the interglacial period known as Marine Isotopic Stage 11 (MIS11), the global temperature was 1 to 2 degrees Celsius greater[2] and sea level was 6 to 13 metres higher[1,3]. Sea level estimates in excess of about 10 metres, however, have been discounted because these require a contribution from the East Antarctic Ice Sheet[3], which has been argued to have remained stable for millions of years before and includes MIS11[4,5]. Here we show how the evolution of ^{234}U enrichment within the subglacial waters of East Antarctica recorded the ice sheet's response to MIS11 warming. Within the Wilkes Basin, subglacial chemical precipitates of opal and calcite record accumulation of ^{234}U (the product of rock–water contact within an isolated subglacial reservoir) up to 20 times higher than that found in marine waters. The timescales of ^{234}U enrichment place the inception of this reservoir at MIS11. Informed by the ^{234}U cycling observed in the Laurentide Ice Sheet, where ^{234}U accumulated during periods of ice stability[6] and was flushed to global oceans in response to deglaciation[7], we interpret our East Antarctic dataset to represent ice loss within the Wilkes Basin at MIS11. The ^{234}U accumulation within the Wilkes Basin is also observed in the McMurdo Dry Valleys brines[8–10], indicating[11] that the brine originated beneath the adjacent East Antarctic Ice Sheet. The marine origin of brine salts[10] and bacteria[12] implies that MIS11 ice loss was coupled with marine flooding. Collectively, these data indicate that during one of the warmest Pleistocene interglacials, the ice sheet margin at the Wilkes Basin retreated to near the precipitate location, about 700 kilometres inland from the current position of the ice margin, which—assuming current ice volumes—would have contributed about 3 to 4 metres[13] to global sea levels.

Large uncertainties in reconstructions of sea level highstands during Earth's past warm interglacial periods, as well as in the predictions of future sea level rise, result in part from the poorly constrained climate sensitivity of the East Antarctic Ice Sheet (EAIS). The EAIS is the world's largest freshwater reservoir and ice loss in response to a warming climate is expected to be focused on the low-elevation basins most susceptible to grounding line retreat, including the Wilkes, Pensacola and Aurora basins[14], which could collectively contribute 8–10 m in sea level rise[15] (Fig. 1). Yet an idea that has prevailed for decades argues that the EAIS has remained stable on million-year timescales[4,5]. The apparent stability of East Antarctica is inferred primarily from the preservation of ancient glacial features, slow erosion and a lack of evidence for major melting within the Transantarctic Mountains[4,5], the polar desert range that borders the EAIS (Fig. 1). Although this result was initially supported by ice-sheet models that required unrealistic warming (>10 °C) to yield ice loss[16], recent models that incorporate ice–ocean interactions do predict an East Antarctic response to modest warming within low-elevation basins, including the Wilkes Basin, while preserving ice in the Transantarctic Mountains[13,14]. The susceptibility of the marine basins to deglaciation has gained support from observations gathered from Pleistocene sediment cores collected offshore of the Wilkes Basin[17]. These data reveal oscillations in the provenance of detrital sediment that have been interpreted to reflect a shift from coastal to on-continent erosion driven by Wilkes Basin ice loss during interglacial periods MIS5, MIS9 and MIS11 that was greater than the ice loss observed in the Holocene. Despite these theoretical advances and observations, which have shifted scientific views towards a more dynamic EAIS, neither the computational models nor offshore sedimentary records are capable of determining both the timing and magnitude of EAIS deglaciation during Pleistocene interglacials. These past interglacial warm periods are characterized by global warming of 1–2 °C above preindustrial temperatures, a substantial warming

[1]Earth and Planetary Sciences, University of California Santa Cruz (UCSC), Santa Cruz, CA, USA. [2]Quaternary Research Center, University of Washington, Seattle, WA, USA. [3]Department of Geology, University of Kansas, Lawrence, KS, USA. ✉e-mail: terryb@ucsc.edu

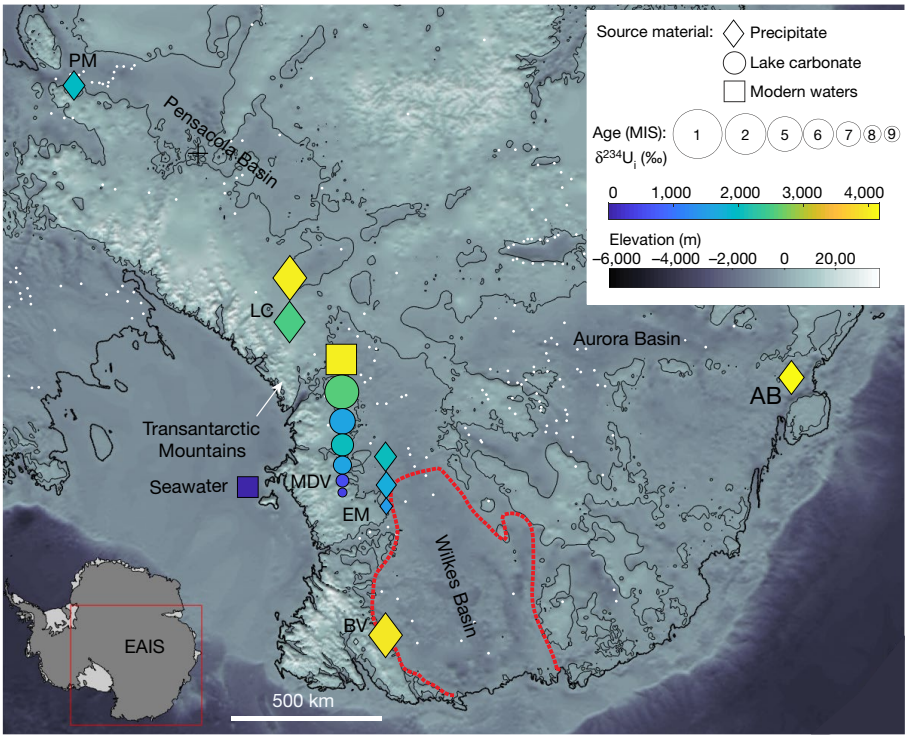

Fig. 1 | Base map of East Antarctica showing bedrock topography. Data are from Bedmap2[39,40] (greyscale contour) overlain by the contour line at sea level (0 m). White dots are known subglacial lakes[41]. The dashed red line shows the model-predicted grounding line in response to 1.8 °C of ocean warming and corresponds to ice volumes equivalent to 3–4 m of sea level rise[13]. Subglacial precipitate locations: PM, Pensacola mountains; LC, Lewis Cliff[25]; EM, Elephant Moraine; BV, Boggs Valley[24]; AB, Aurora Basin[26]; and MDV, McMurdo Dry Valleys[8–10](contemporary waters and lake carbonates). SW, seawater[8]. Data point size indicates age, and colour indicates $\delta^{234}U_i$ composition.

increase that is analogous to projected near-future climate change[1]. Thus, any additional means of recognizing the timing and magnitude of past ice-loss events in East Antarctica in response to warming may clarify the height of sea level highstands in both the past and future.

Such additional methods for documenting ice sheet collapse have recently been developed by Chen and others[7] who showed that the collapse of the Laurentide ice sheet 15–20 thousand years ago (ka) was associated with a transient 3‰ increase in the $\delta^{234}U$ (where $\delta^{234}U = [(^{234}U/^{238}U)_{AR} - 1] \times 1{,}000$) composition of Atlantic waters relative to modern seawater. Aqueous enrichment in ^{234}U above secular equilibrium ($\delta^{234}U = 0$‰) reflects rock–water interaction[18] and in glacial systems may be attributed to the recoil injection of ^{234}U into basal ice and subglacial waters incurred during the α-decay of parent ^{238}U housed within debris-laden basal ice and subglacial sediments (Fig. 2, bottom inset). From the change in ocean water compositions, Chen and others[7] inferred that a reservoir strongly enriched in ^{234}U within the Laurentide ice sheet was flushed rapidly into the ocean during early phases of the last glacial termination. They pointed to the brines of the McMurdo Dry Valleys, Antarctica, which currently exhibit $\delta^{234}U$ compositions greater than 3,000‰ (refs. [8,10]), as a possible analogue to the Laurentide ^{234}U-enriched reservoir.

Results

Here we report results from a new Antarctic archive of $\delta^{234}U$ compositions: chemical precipitates formed in subglacial aquatic environments beneath the EAIS. These aqueous chemical precipitates form as a byproduct of subglacial freezing, a process that consumes subglacial waters, concentrating solutes to the point of calcite[19,20] or amorphous silica/opal[21,22] precipitation. The oxygen compositions of Antarctic calcite precipitates are among the most ^{18}O-depleted compositions on Earth[20,23,24], which confirms their precipitation from Antarctic subglacial waters[23]. Precipitates sampled from either deglaciated bedrock surfaces[23,24] or from exposed sections of basal ice or moraines[20,25] place the location of precipitate formation beneath the ice. Because they can be dated by ^{234}U–^{230}Th methods (see Methods), these precipitates record the $\delta^{234}U$ of subglacial waters at the time of sample precipitation ($\delta^{234}U_i$) and collectively reveal that ^{234}U enrichment is not limited to the waters of the McMurdo Dry Valleys alone, but rather, is observed to be both geographically and temporally ubiquitous in the aquatic environments of East Antarctica (Fig. 1).

Figure 1 shows the distribution of both new (Extended Data Table 1) and existing[24–26] U-series data for five EAIS precipitate locations, four of which border the EAIS along the Transantarctic Mountains within the Pensacola and Wilkes basins; the fifth lies within the Aurora basin. Precipitates from each of these locations exhibit $\delta^{234}U_i$ compositions well in excess of secular equilibrium and marine compositions ($\delta^{234}U = 145$‰ (ref. [27]), Fig. 1). These observations imply that subglacial waters are the source and cause of change in marine $\delta^{234}U$ (ref. [7]) 15–20 ka and inform us that basal waters from the Laurentide ice sheet were flushed in advance of large-scale deglaciation. A comparison between the ^{234}U–^{230}Th date and the $\delta^{234}U_i$ for EAIS precipitates yields an apparent shared history for this continent-scale compilation that is characterized by ^{234}U accumulation, with $\delta^{234}U_i$ increasing by >2,000‰ over the past 300 ka or so (Fig. 3). Part of this long-term archive of ^{234}U accumulation is recorded in a single geographic location by a subglacial precipitate sample from Elephant Moraine (PRR50489). This centimetre-thick sample of layered opal and calcite has been dated at multiple horizons, revealing ^{234}U–^{230}Th dates from 265 ka to 150 ka and record changes of $\delta^{234}U_i$ within the subglacial waters of the Wilkes subglacial basin of >700‰ (Fig. 3). An additional sample from Elephant Moraine (PRR39222) also exhibits variations in $\delta^{234}U$ with stratigraphic position. Though low U/Th for PRR39222 inhibits a reliable age determination, the measured $\delta^{234}U$ values, uncorrected for ^{234}U decay, are approximately 40–140‰

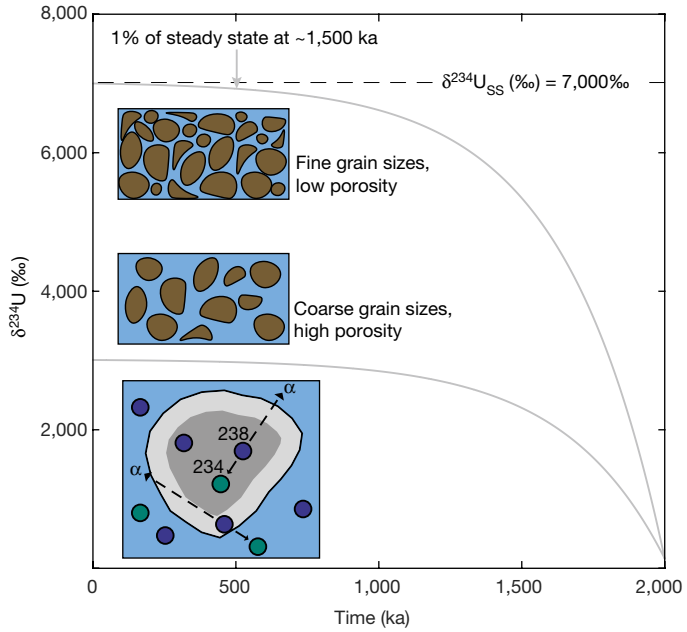

Fig. 2 | Model ^{234}U ingrowth histories in waters from injection by α recoils from the decay of ^{238}U housed within sediments. The ^{234}U system reaches within 1% of steady state before approximately 1,500 ka, after which time the $\delta^{234}U_i$ recorded by precipitates would remain constant over time. If changes in $\delta^{234}U_i$ over time are observed, this requires: (1) lower δ^{234}U starting fluids and (2) isolation to permit ^{234}U accumulation. Differences in sediment characteristics (for example, porosity and U content) can vary across a continent, thus producing a range in $\delta^{234}U_{SS}$.

and correlate with stratigraphic position (the top corresponds to higher δ^{234}U, Extended Data Table 1). With the formation time unknown, we can instead model the $\delta^{234}U_i$ values for formation 0–450 ka for both the top and bottom of the sample (Fig. 3, purple curves). If we assume sample precipitation rates (0.5–5 mm kyr^{-1}) similar to Antarctic calcite dated by U–Th methods (for example, PRR50489) we can define a formation duration for PRR39222 (45 mm) of about 10–90 kyr. Assuming these durations, along with the requirement that the bottom and top of the sample intersect the purple curves shown in Fig. 3, permits the definition of possible $\delta^{234}U_i$ ingrowth (that is, the production and accumulation of radiogenic daughter products) histories (black arrows, Fig. 3). We find that possible ingrowth histories are congruent with the shared $\delta^{234}U_i$ ingrowth history for the region if this sample formed about 400 ka (Extended Data Fig. 3) but incongruent at earlier formation times (Extended Data Fig. 3). Although uncertainty on the age of PRR39222 remains, the occurrence of low δ^{234}U (<500‰) in subglacial fluids is apparently rare (Fig. 3), having been identified in this region only in samples older than about 300 kyr (with the exception of a single outlier in the Taylor Valley dataset). This suggests that PRR39222 records the ingrowth of ^{234}U within Wilkes Basin waters at about 300–400 ka.

As introduced above, ^{234}U enrichment has been recorded in waters of the McMurdo Dry Valleys. The McMurdo Dry Valleys are the largest ice-free area of Antarctica, where land-terminating glaciers permit subglacial brines to emanate onto the surface or into proglacial lakes[11]. The source of McMurdo Dry Valleys fluids has been extensively studied: the geochemistry[10], isotopic composition[28] and bacterial ecosystems[12] all point to origination from a marine flooding event that occurred before isolation of fluids from the atmosphere on timescales greater than 200 kyr[29,30] (see Methods for further discussion). Citing observations of ancient preserved features and slow erosion within the Transantarctic Mountains[4,5], the timing of the marine incursion associated with McMurdo Dry Valleys brines has often been relegated to occurring millions of years ago in the warmer Miocene climate[10,12]. Modern McMurdo Dry Valleys brines and surface lakes found in both the Taylor and Wright valleys, however, are observed to share characteristics with fluids beneath the EAIS: they are currently strongly enriched in ^{234}U (Fig. 1, δ^{234}U > 3,000‰)[8,10]. Carbonates that formed within past proglacial lakes of Taylor Valley also record elevated δ^{234}U values[9], suggesting that these palaeolakes, like modern Lake Bonney[11], were also fed by subglacial waters. Similar to the subglacial precipitates in the EAIS, we note that the existing data for these McMurdo Dry Valleys lake carbonates document an increase in $\delta^{234}U_i$ over the past 300 kyr or so (Fig. 3a). This coevolution of δ^{234}U in McMurdo Dry Valleys and EAIS fluids supports the view that McMurdo Dry Valleys brines formed much more recently than the Miocene and have been sourced from subglacial EAIS fluids within the Wilkes Basin that have been cryoconcentrated in transit by subglacial freezing[11].

The accumulation to high values (>3,000‰) and the evolution of $\delta^{234}U_i$ with time as recorded by EAIS precipitates, McMurdo Dry Valleys lake carbonates and modern fluids both match the model predictions of ^{234}U ingrowth by direct injection into fluids during the decay of ^{238}U housed within subglacial sediments (Fig. 2 and Supplementary Information). Collectively, these data point to a subglacial water reservoir starting with low δ^{234}U compositions that have increased by ^{234}U recoil ejection from sediments but that has not yet reached a steady-state δ^{234}U composition ($\delta^{234}U_{SS}$), which is attained after >1 million years of rock–water contact (Fig. 2). To place an estimate on the duration of rock–water contact, we employ a model that simulates ^{234}U ingrowth histories from α recoils and explores two key variables: the onset time and the $\delta^{234}U_{SS}$ (see Supplementary Information). A number of physical variables influence the rate of ^{234}U ingrowth and $\delta^{234}U_{SS}$, including sediment grain size, uranium content and porosity (Fig. 2). For the purposes of estimating the timing of reservoir inception, we need not uniquely determine any of these reservoir traits which, given their occurrence beneath the EAIS, are poorly known. Rather, we can explore extreme ranges of all variables via their net effect on $\delta^{234}U_{SS}$ and identify, using a maximum likelihood test, the model ingrowth histories that best match the measured data. However, it is expected that the physical traits controlling ^{234}U accumulation differ from one subglacial reservoir to the next (Fig. 2). For example, the approximately 2,000‰ range in δ^{234}U observed between modern waters and young (<25 kyr) precipitates from across East Antarctica probably reflects differences in the sediment characteristics between these geographically and geologically distinct regions (Fig. 3). This heterogeneity does not apply to sample PRR50489, a centimetre-thick sample that provides a >100-kyr record of ^{234}U accumulation beneath the ice in a single location. Using a maximum-likelihood test, we compare the measured results for PRR50489 with model simulations of ^{234}U ingrowth for a range of reservoir isolation times (100–800 kyr), initial δ^{234}U (that is, $\delta^{234}U_i$) for the subglacial reservoir (0–1,500‰) and $\delta^{234}U_{SS}$ (2,000–9,000‰). The uncertainty in the timing of reservoir isolation is dominated by the possible range of $\delta^{234}U_i$ compositions for the reservoir. Assuming values as low as those observed in sample PRR39222 or marine compositions (145‰), best-fit paths correspond to reservoir inception times of 435^{+20}_{-25} ka (95% confidence interval, $\chi_v^2 = 3.9$) (Fig. 3b, c). If the reservoir were initially enriched in ^{234}U, perhaps up to 500‰ as in the oldest carbonates found in Taylor Valley, the best-fit path is shifted with an inception time of 390^{+25}_{-15} ka (95% confidence interval, $\chi_v^2 = 3.9$) (Fig. 3c). Thus, even assuming a range of $\delta^{234}U_i$ compositions that lie between sample PRR39222 and the oldest Taylor Valley carbonates, we identify a reservoir inception time coincident with MIS11. In contrast, for reservoir isolation to have begun during the next interglacial (MIS9) would require a $\delta^{234}U_i$ in subglacial waters of >1,000‰ (Fig. 3c), consistent with the lowest values observed in Elephant Moraine sample PRR50489. The formation of subglacial samples during subsequent interglacials (MIS5, MIS7), along with documented ^{234}U accumulation during these times, is inconsistent with MIS5 or MIS7 ice loss and instead point to

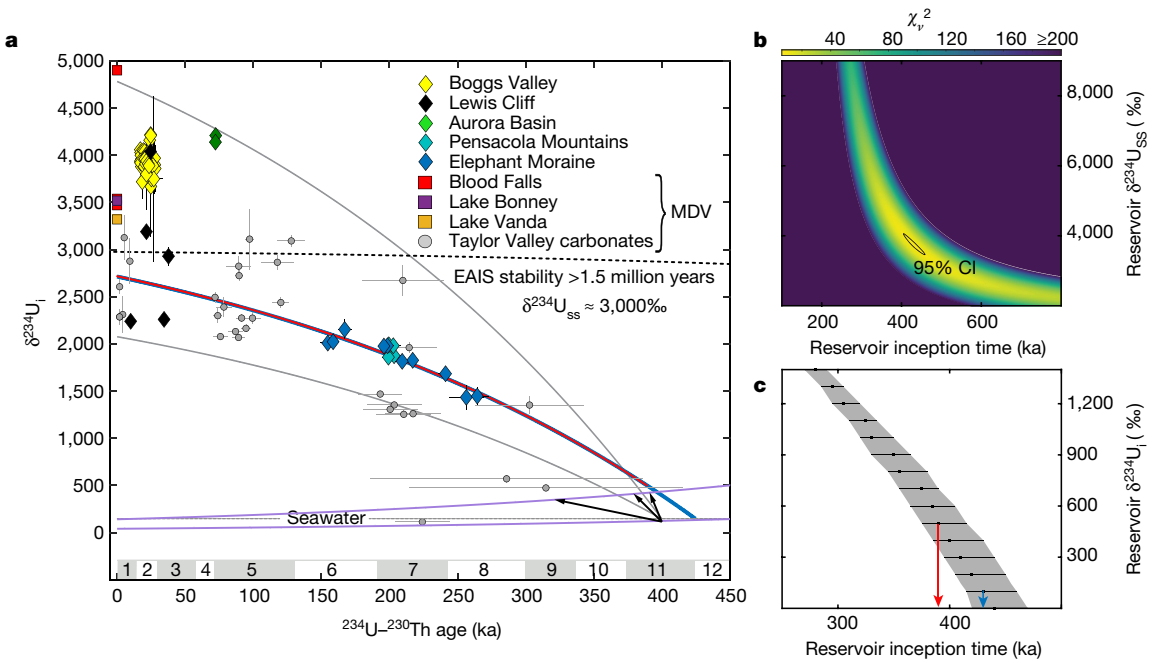

Fig. 3 | Measured and modelled ^{234}U ingrowth histories for the Wilkes Basin. **a**, Formation age versus the $\delta^{234}U_i$ for EAIS subglacial precipitates, McMurdo Dry Valleys (MDV) waters and lake carbonates. The timescale above the *x* axis corresponds to MIS numbers. See Fig. 1 for locations. All measurement uncertainties (both horizontal and vertical) are ±2*σ*. The blue and red curves correspond to maximum-likelihood modelled ingrowth curves for the Elephant Moraine sample PRR50489, where the colour indicates the $\delta^{234}U_i$ of a subglacial reservoir: 500‰ (red) and 100‰ (blue), which correspond to the lowest compositions observed in Taylor Valley and Elephant Moraine (PRR39222), respectively. Purple lines show the calculated $\delta^{234}U_i$ for PRR39222 over 0–450 ka with superimposed $\delta^{234}U$ ingrowth histories (black arrows) from assumed calcite precipitation rates (see Extended Data Fig. 3 for further discussion). Grey curves show the model projections for scenarios with a 400-ka onset and variations in sediment characteristics from Fig. 2. The dashed line in **a** shows the prediction for a ^{234}U system after about 1 My of rock–water contact. The example maximum-likelihood estimate in **b** assumes a $\delta^{234}U_i$ for the reservoir of 145‰ and identifies a best-fit path with an inception time of 435^{+20}_{-25} ka (95% confidence interval, CI; black uncertainty ellipse). **c**, Uncertainty in reservoir inception time is dominated by the $\delta^{234}U_i$ of the hydrologic reservoir. The grey polygon outlines the 95% confidence envelope of the best-fit conditions. Independently of the $\delta^{234}U_i$ of the reservoir, the best-fit curves identify near-identical ingrowth histories and $\delta^{234}U_{ss}$ (overlapping blue and red curves shown in **a**).

an earlier reservoir isolation that permits ^{234}U to accumulate to the values observed.

Discussion and conclusions

Measured data from both EAIS precipitates and carbonates from the McMurdo Dry Valleys unequivocally record ^{234}U accumulation within fluids that initiated at $\delta^{234}U$ values lower than present (Fig. 3). Our documented accumulation does not reflect a ^{234}U system in steady state (black dashed line, Fig. 3) and are thus inconsistent with fluids that have experienced isolation and contact with rocks on million-year durations. Collectively, these observations are inconsistent with models for extreme EAIS stability on million-year timescales. Rather, these data require that the subglacial reservoir within the low-elevation Wilkes Basin began at a lower $\delta^{234}U$ and remained at least partially isolated with respect to uranium for only about 400 kyr. Without such isolation ^{234}U would not have accumulated, requiring that over the past 400 kyr or so, the evacuation and replacement of ^{234}U-enriched fluids from the ice sheet base was exceeded by ^{234}U enrichment. The accumulation of ^{234}U in this isolated to partially isolated reservoir implies ice stability over the past 400 kyr. The lower $\delta^{234}U$ values inferred at MIS10 to MIS11, however, imply that the replacement of ^{234}U-enriched fluids, perhaps by flushing of basal waters or ice cap retreat, did outpace ^{234}U ingrowth at this time. This interpretation of the ^{234}U accumulation record in East Antarctica draws on the observed ^{234}U cycling in the Laurentide ice sheet, where ^{234}U-enriched subglacial waters were documented at the peak of Laurentide ice extent/volume (25 ka)[6], but the reservoir was released to global oceans in response to deglaciation[7]. Although any record of ^{234}U accumulation beneath the EAIS before MIS11 is not reflected in the data presented here, we may infer from the documentation of ^{234}U enrichment beneath the Laurentide[6,7], Cordilleran[22], Iceland[31], Greenland[32] and Antarctic ice masses that ^{234}U accumulation occurs in response to protracted rock–water contact in an isolated or partially isolated reservoir. On the basis of the documented response in Atlantic coral $\delta^{234}U_i$ to Laurentide deglaciation[7], we suggest that any pool of pre-MIS11 ^{234}U-rich waters stored beneath the EAIS as well as Greenland and West Antarctica (see below) was released to the oceans, which may explain, in conjunction with diagenetic effects, why the $\delta^{234}U_i$ compositions of MIS11 corals record a change in marine $\delta^{234}U_i$ compositions[33] a factor of ten greater than the change recorded[7] in response to the most recent deglaciation .

There are few possible ice-sheet responses to MIS11 warming that may have led to the observed cycling in $\delta^{234}U$. Increased warming could have led to enhanced glacial ablation on the EAIS, complete with surface melting, moulin formation and flushing basal waters that reset the ^{234}U accumulation at the base of the ice. The basal flushing volumes required to lower the $\delta^{234}U$ within subglacial waters are 3–4 orders of magnitude higher than estimates of present-day subglacial water volumes (Extended Data Fig. 5, Methods and Supplementary Information). The question arises of whether MIS11 warming was sufficient to induce such surface melting and meltwater penetration to the bed, within the Wilkes Basin. Ice-sheet models[14] and our current climate do not support this response and instead show that EAIS retreat within the marine basins would have to be driven by ocean–ice interactions, which would

occur before sufficient warming to permit surface melting and basal flushing at such high volumes. In short, polar conditions like today's would have persisted on the ice surface even as the ice mass retreated within the low-elevation marine basins in response to warming oceans.

Thus, an alternative explanation to basal flushing for the observed cycling in $\delta^{234}U$ is that the Wilkes Basin grounding line moved closer to the precipitate sampling locations during MIS11 as a result of ice interaction with warming oceans (Fig. 1). Under such a mechanism for removal of ^{234}U-enriched waters, the geographic position of subglacial precipitates could be used to infer whether ice in a specific location remained stable or was lost at a particular point in time. For example, the Elephant Moraine samples derive from a glacial catchment that extends into the Wilkes Basin about 700 km inboard of the current grounding line (Fig. 1). The loss of ^{234}U at this location implies substantial retreat within the Wilkes Basin at MIS11. Such a collapse is plausible: the inland-sloping topography of Wilkes Basin makes grounding-line retreat in this region susceptible to a positive feedback that could produce more than 800 km of grounding-line migration[13]. And while basal flushing and grounding-line retreat could work hand-in-hand to some extent, the width of an ablation zone within a retreating ice sheet at high latitudes would be sufficiently narrow (<30 km)[34,35] to render the relative contribution of flushing to resetting ^{234}U accumulation relatively minor when compared to the hundreds of kilometres of grounding-line migration required to affect the samples studied here. In other words, these samples are so far inland, and the conditions are still so cold, that grounding-line retreat must be the dominant mechanism for ^{234}U resetting.

If ice retreated from Wilkes Basin, which lies below sea level, it would fill with seawater, replacing or mixing with high-$\delta^{234}U$-composition waters. Following MIS11, the subsequent re-advance of ice over marine sediments with connate seawater would impart marine signatures to subglacial waters, consistent with the geochemical, isotopic and biogeochemical evidence for marine sourcing of McMurdo Dry Valleys fluids[10,12]. In addition, proposed ice loss in MIS11 within the Wilkes Basin is consistent with glaciological evidence and with maximum meteorite terrestrial ages at the Elephant Moraine of around 400 kyr (see Methods for further discussion). The accumulation of ^{234}U at the Elephant Moraine throughout MIS5, MIS7 and very likely MIS9 (Fig. 1) suggests that any ice loss during these shorter-duration warmer periods, as resolved by offshore sedimentary records[17], did not reach this far back into the Wilkes Basin.

Indeed, offshore sedimentary archives record a more pronounced on-continent weathering signal during MIS11 than in subsequent interglacials[17]. At the warmer and longer MIS11 interglacial the EAIS grounding line must have retreated to the proximity of the Elephant Moraine, about 700 km inland from the current coastline. A minimum contribution of Wilkes Basin collapse to global sea level at MIS11 can be estimated if we assume that: (1) grounding-line retreat was not accompanied by ice-sheet thickening, as invoked for warmer Pliocene conditions[36], and (2) ice volumes before MIS11 warming were at least comparable with the current, well known ice volumes[13]. Both assumptions are probably safe. Models predict[36] ice thickening during Pliocene warmth where low sea-ice coverage leads to increased precipitation, conditions that do not apply to the colder Pleistocene. Similarly, ice volumes within the Wilkes Basin before MIS11 warming are likely to be comparable or greater than at present. Preceding MIS11 warming, MIS12 was one of the coldest glacial periods of the Pleistocene[2], whereas currently, during one of the warmest Pleistocene interglacials, the basin contains ice volumes that would contribute an estimated 3–4 m (ref. [13]) to global sea level rise in response to the reported extent of Wilkes Basin grounding-line retreat.

The record presented here tightly brackets the EAIS response to a warming world: 1–2 °C warming during the long MIS11 interglacial, with the warmest temperatures observed since about 2 million years ago, resulted in hundreds of kilometres of grounding-line retreat, while similar temperatures during the subsequent and shorter MIS5 and MIS9 interglacials did not result in a comparable retreat. Our interpretation of a diminished MIS11 ice sheet in the Wilkes Basin that contributed several metres to global sea level is also consistent with distal geologic data for the sea level during this interglacial. Sea-level reconstructions resulting from MIS11 warming are up to 4 m higher than the subsequent interglacials, suggesting that the Wilkes Basin may account for the difference in sea-level highstands. The MIS11 highstands of 6–13 m[3] have been attributed to the near-complete collapse of the Greenland (4.5–6 m; ref. [37]) and West Antarctic (3.2–5 m; ref. [38]) ice sheets alone[3], which can account for a maximum of only 11 m. The 700 km of grounding-line retreat reported here would very probably result in several metres of global sea-level rise, suggesting that MIS11 highstands greater than 11 m and perhaps as high as 13 m may occur in response to 1–2 °C of global warming.

Online content

Any methods, additional references, Nature Research reporting summaries, source data, extended data, supplementary information, acknowledgements, peer review information; details of author contributions and competing interests; and statements of data and code availability are available at https://doi.org/10.1038/s41586-020-2484-5.

1. Dutton, A. et al. Sea-level rise due to polar ice-sheet mass loss during past warm periods. *Science* **349**, aaa4019 (2015).
2. Lisiecki, L. E. & Raymo, M. E. A Pliocene-Pleistocene stack of 57 globally distributed benthic $\delta^{18}O$ records. *Paleoceanogr. Paleoclimatol.* **20**, PA1003 (2005).
3. Raymo, M. E. & Mitrovica, J. X. Collapse of polar ice sheets during the stage 11 interglacial. *Nature* **483**, 453–456 (2012).
4. Sugden, D. E., Marchant, D. R. & Denton, G. H. The case for a stable East Antarctic ice sheet: the background. *Geogr. Ann. Ser. A* **75**, 151–154 (1993).
5. Sugden, D. E. et al. Preservation of Miocene glacier ice in East Antarctica. *Nature* **376**, 412–414 (1995).
6. Refsnider, K. A. et al. Subglacial carbonates constrain basal conditions and oxygen isotopic composition of the Laurentide Ice Sheet over Arctic Canada. *Geology* **40**, 135–138 (2012).
7. Chen, T. et al. Ocean mixing and ice-sheet control of seawater $^{234}U/^{238}U$ during the last deglaciation. *Science* **354**, 626–629 (2016).
8. Henderson, G. M., Hall, B. L., Smith, A. & Robinson, L. F. Control on ($^{234}U/^{238}U$) in lake water: a study in the Dry Valleys of Antarctica. *Chem. Geol.* **226**, 298–308 (2006).
9. Hendy, C. H., Healy, T. R., Rayner, E. M., Shaw, J. & Wilson, A. T. Late Pleistocene glacial chronology of the Taylor Valley, Antarctica, and the global climate. *Quat. Res.* **11**, 172–184 (1979).
10. Lyons, W. B. et al. The geochemistry of englacial brine from Taylor Glacier, Antarctica. *J. Geophys. Res. Biogeosci.* **124**, 633–648 (2019).
11. Mikucki, J. A. et al. Deep groundwater and potential subsurface habitats beneath an Antarctic dry valley. *Nat. Commun.* **6**, 6831 (2015).
12. Mikucki, J. A. & Priscu, J. C. Bacterial diversity associated with Blood Falls, a subglacial outflow from the Taylor Glacier, Antarctica. *Appl. Environ. Microbiol.* **73**, 4029–4039 (2007).
13. Mengel, M. & Levermann, A. Ice plug prevents irreversible discharge from East Antarctica. *Nat. Clim. Chang.* **4**, 451–455 (2014).
14. DeConto, R. M. & Pollard, D. Contribution of Antarctica to past and future sea-level rise. *Nature* **531**, 591–597 (2016).
15. Gasson, E., DeConto, R. & Pollard, D. Antarctic bedrock topography uncertainty and ice sheet stability. *Geophys. Res. Lett.* **42**, 5372–5377 (2015).
16. Huybrechts, P. Glaciological modelling of the Late Cenozoic East Antarctic ice sheet: stability or dynamism? *Geogr. Ann. Ser. A* **75**, 221–238 (1993).
17. Wilson, D. J. et al. Ice loss from the East Antarctic Ice Sheet during late Pleistocene interglacials. *Nature* **561**, 383–386 (2018).
18. Kigoshi, K. Alpha-recoil thorium-234: dissolution into water and the uranium-234/uranium-238 disequilibrium in nature. *Science* **173**, 47–48 (1971).
19. Hallet, B. Deposits formed by subglacial precipitation of $CaCO_3$. *Geol. Soc. Am. Bull.* **87**, 1003–1015 (1976).
20. Faure, G., Hoefs, J., Jones, L. M., Curtis, J. B. & Pride, D. E. Extreme ^{18}O depletion in calcite and chert clasts from the Elephant Moraine on the East Antarctic ice sheet. *Nature* **332**, 352–354 (1988).
21. Hallet, B. Subglacial silica deposits. *Nature* **254**, 682–683 (1975).
22. Blackburn, T. et al. Composition and formation age of amorphous silica coating glacially polished surfaces. *Geology* **47**, 347–350 (2019).
23. Aharon, P. Oxygen, carbon and U-series isotopes of aragonites from Vestfold Hills, Antarctica: clues to geochemical processes in subglacial environments. *Geochim. Cosmochim. Acta* **52**, 2321–2331 (1988).
24. Frisia, S. et al. The influence of Antarctic subglacial volcanism on the global iron cycle during the Last Glacial Maximum. *Nat. Commun.* **8**, 15425 (2017).
25. Fitzpatrick, J. J., Muhs, D. R. & Jull, A. J. T. Saline minerals in the Lewis Cliff ice tongue, Buckley Island quadrangle, Antarctica. *Contrib. Antarctic Res. I* **50**, 57–69 (1990).

26. Goodwin, I. D. et al. Modern to Glacial age subglacial meltwater drainage at Law Dome, coastal East Antarctica from topography, sediments and jökulhlaup observations. *Geol. Soc. Lond. Spec. Publ.* **461**, 215–230 (2018).
27. Chutcharavan, P. M., Dutton, A. & Ellwood, M. J. Seawater $^{234}U/^{238}U$ recorded by modern and fossil corals. *Geochim. Cosmochim. Acta* **224**, 1–17 (2018).
28. Berry Lyons, W., Frape, S. K. & Welch, K. A. History of McMurdo Dry Valley lakes, Antarctica, from stable chlorine isotope data. *Geology* **27**, 527–530 (1999).
29. Poreda, R. J., Hunt, A. G., Lyons, W. B. & Welch, K. A. The helium isotopic chemistry of Lake Bonney, Taylor Valley, Antarctica: timing of late Holocene climate change in Antarctica. *Aquat. Geochem.* **10**, 353–371 (2004).
30. Warrier, R. B., Castro, M. C., Hall, C. M., Kenig, F. & Doran, P. T. Reconstructing the evolution of Lake Bonney, Antarctica using dissolved noble gases. *Appl. Geochem.* **58**, 46–61 (2015).
31. Pogge von Strandmann, P. A. E. et al. Riverine behaviour of uranium and lithium isotopes in an actively glaciated basaltic terrain. *Earth Planet. Sci. Lett.* **251**, 134–147 (2006).
32. Arendt, C. A. et al. Influence of glacial meltwater on global seawater $\delta^{234}U$. *Geochim. Cosmochim. Acta* **225**, 102–115 (2018).
33. Bard, E., Fairbanks, R. G., Hamelin, B., Zindler, A. & Hoang, C. T. Uranium-234 anomalies in corals older than 150,000 years. *Geochim. Cosmochim. Acta* **55**, 2385–2390 (1991).
34. Catania, G. A., Neumann, T. A. & Price, S. F. Characterizing englacial drainage in the ablation zone of the Greenland ice sheet. *J. Glaciol.* **54**, 567–578 (2008).
35. Bøggild, C. E., Brandt, R. E., Brown, K. J. & Warren, S. G. The ablation zone in northeast Greenland: ice types, albedos and impurities. *J. Glaciol.* **56**, 101–113 (2010).
36. Yamane, M. et al. Exposure age and ice-sheet model constraints on Pliocene East Antarctic ice sheet dynamics. *Nat. Commun.* **6**, 7016 (2015).
37. Reyes, A. V. et al. South Greenland ice-sheet collapse during marine isotope stage 11. *Nature* **510**, 525–528 (2014).
38. Gomez, N., Mitrovica, J. X., Tamisiea, M. E. & Clark, P. U. A new projection of sea level change in response to collapse of marine sectors of the Antarctic Ice Sheet. *Geophys. J. Int.* **180**, 623–634 (2010).
39. Fretwell, P. et al. Bedmap2: improved ice bed, surface and thickness datasets for Antarctica. *Cryosphere* **7**, 375–393 (2013).
40. Greene, C. A., Gwyther, D. E. & Blankenship, D. D. Antarctic Mapping Tools for Matlab. *Comput. Geosci.* **104**, 151–157 (2017).
41. Pattyn, F. Antarctic subglacial conditions inferred from a hybrid ice sheet/ice stream model. *Earth Planet. Sci. Lett.* **295**, 451–461 (2010).

Methods

U-series methods

^{234}U–^{230}Th dates were produced at the University of California Santa Cruz (UCSC) Keck Isotope Laboratory. Sample digestions were carried out using either 7N HNO_3 (calcite) or concentrated HF + HNO_3 (opal). Samples were spiked with a gravimetrically calibrated mixed ^{229}Th–^{236}U tracer and dried down. U and Th separates were purified using an ion chromatography procedure that used 1 ml of AG1-X8 anion resin. Total procedural blanks for U and Th were <5 pg and minor relative to sample sizes. Uranium isotopic measurements were conducted using the IsotopX X62 Thermal Ionization Mass Spectrometer (TIMS) housed at UCSC and measured uranium as UO_2 using a Si-gel emitter. Uranium compositions were corrected for oxide isobaric interferences following ref. [42]. Mass-dependent fractionation correction was applied using a linear correction with the correction factor determined from long-term measurement of standards. Uranium dead times for the Daly were calibrated using NBS U-500. Accuracy of the uranium method was evaluated using the uranium standard NBS4321. Extended Data Fig. 4 shows NBS4321 analyses measured over the duration of this study. Thorium isotopic determinations used the UCSC TIMS, by graphite loading and a Daly peak hopping routine. Thorium fractionation and dead time were estimated by running NBS U 500 as a metal. ^{234}U–^{230}Th date accuracy was tested using MIS5e coral dated by Hamelin and others[43], an in-house opal standard in secular equilibrium and subglacial carbonate precipitate previously dated by Frisia et al.[24] (Extended Data Table 3). U–Th ages are calculated using codes designed at UCSC. Decay constants for all data and models were from Cheng et al.[44]. All uncertainties are reported at 2σ. Mass spectrometry methods are described in greater detail in Supplementary Information.

Simulating porewater $\delta^{234}U$ evolution

The $\delta^{234}U$ enrichment in subglacial settings could result from direct injection or preferential leaching of ^{234}U from glacial sediments into subglacial waters. Preferential leaching of ^{234}U relative to ^{238}U has experimentally been shown to increase fluid $\delta^{234}U$ to marine-like compositions on laboratory timescales; however, there is a finite pool of leachable ^{234}U in rocks, such that on longer residence times (>10^4 yr) both natural and experimental waters reveal submarine $\delta^{234}U$ (ref. [45]). In the EAIS, however, the accumulation to high $\delta^{234}U$ values (4,000‰) and the topology of $\delta^{234}U_i$ with time both match the model predictions of ^{234}U accumulation by direct injection into fluids incurred during the decay of ^{238}U housed within subglacial sediments. Collectively, these data point to a subglacial water reservoir that initiated with low $\delta^{234}U$ compositions and then increased by ^{234}U recoil injection but has yet to reach the $\delta^{234}U_{SS}$ value that the ^{234}U system would attain after approximately a million years of rock–water contact. The time-dependent evolution of ^{234}U in sediment porewaters may be described by a model presented in Supplementary Information. Using this model, simulated $^{234}U/^{238}U$ fluid evolutions are evaluated by comparison with the measured data using a maximum-likelihood test (also detailed in Supplementary Information).

Influence of hydrological flushing on $\delta^{234}U$ of subglacial waters

Our analyses of subglacial precipitates record a progressive increase in $\delta^{234}U$ of subglacial waters, from which these precipitates formed, since MIS11, when the $\delta^{234}U$ reservoir has been reset to very low values. We consider here (and within Supplementary Information, where the model is described in full with equations) whether this MIS11 resetting event may have had to do simply with an increase in basal melting, for example, caused by thickening of the ice sheet due to a warming-induced increase in precipitation[46], and the associated increase in hydrological flushing rates of the subglacial water reservoir. The results of this model show that only very short flushing timescales, of <10 years, result in low values of the steady-state activity ratio. We expect that comparably low values were reached during the event that reset the $\delta^{234}U$ values during MIS11 (Fig. 3). This result applies to other combinations of parameters beyond the ones illustrated in Extended Data Fig. 5. For instance, similar curves can be obtained for a weathering timescale of ten million years as long as the ^{234}U ejection factor is about ten times larger than the values shown in Extended Data Fig. 5, which would require finer-grained subglacial sediments. It is useful at this point to estimate, for reference, what is the flushing rate for the subglacial zone of the modern Antarctic ice sheet. Pattyn[41] used a numerical ice-sheet model to calculate that basal melting produces approximately 65 km^3 of melt per year. Assuming no large change in subglacial water storage and allowing for some losses to infiltration into deep groundwater systems (for example, see ref. [47]) and to basal freezing, this means that the continental-scale hydrological throughflow rate is approximately a few tens of cubic kilometres per year. Dowdeswell and Siegert[48] estimated that subglacial Antarctic lakes alone contain about 10,000 km^3. Another large water reservoir that is hydrologically connected to the basal meltwater system is the porewater in subglacial tills that exchanges chemical species through Darcian flow, physical deformation accompanying ice sheet motion, and ionic diffusion (for example, see ref. [49]). It would require a till layer less than 2 m thick on average across the entire base of the ice sheet for the porewater reservoir to amount to an additional 10,000 km^3 of subglacial storage, assuming reasonable porosity of 35%. Hence, the total subglacial water storage is similar to a few tens of thousands of cubic kilometres. Dividing this volume by the throughflow rate of a few tens of cubic kilometres per year yields an approximate flushing timescale for the modern Antarctic ice sheet of about 1,000 yr. According to Extended Data Fig. 5, such a timescale would allow a build-up of steady-state U^{234} activity ratios comparable to the ones observed in our samples (thousands of ‰). However, the flushing timescale would have to be lowered by about 2–3 orders of magnitude, to 1–10 years, to bring the $\delta^{234}U_{SS}$ to values as low as a few hundred ‰. Although, for simplicity, we have focused here on the discussion of the $\delta^{234}U_{SS}$, we have also performed calculations of the time evolution of $\delta^{234}U$ for a large range of the control parameters f, τ_f and τ_w. We find that the flushing timescale is the predominant timescale that controls the rate of $\delta^{234}U$ convergence towards its steady-state value. This is particularly the case when the flushing timescale is much shorter than the mean lifetime of ^{234}U ($\tau_f \ll \tau_4 = 354{,}260$ yr) because the time-dependent, exponential terms in equations (8) and (10) are either dependent on $1/\tau_f$ or on the sum $(1/\tau_f + 1/\tau_4)$. When the flushing timescale is short, the $1/\tau_4$ term becomes negligibly small and the evolution of $\delta^{234}U$ with time depends only on exponential terms governed by t/τ_f. This means that a decrease in the flushing timescale to small values, for example, 1–10 yr, from a larger value (for example, between 100 yr and 10,000 yr) would very quickly bring the subglacial $\delta^{234}U$ close to its new and lower steady-state value. For instance, $\delta^{234}U$ would be within 5% of the steady-state value after only 3–30 yr have elapsed following the decrease of the flushing timescale to 1–10 yr.

There is no reason to suspect that the total volume of water stored beneath the ice sheet was lower by 2–3 orders of magnitude during MIS11 than today. In fact, this volume is unlikely to change much through time and temporal variations in the flushing timescale must be largely controlled by variations in the water throughflow rate, which would have to increase by 2–3 orders of magnitude compared to today to substantially lower subglacial $\delta^{234}U$. Hence, the ice-sheet base would have to be flushed at the rate of approximately 1,000–10,000 km^3 per year as compared to the modern rate of around 10 km^3 per year. This kind of increase cannot be attributed to an increase in basal melting rate, say, due to ice-sheet thickening during MIS11, which at most could increase the throughflow rate by a small factor, for example, a factor of two. The only process that can introduce enough water to the ice sheet base to lower the flushing timescale by a few orders of magnitude is the penetration of surface meltwater to the ice base through moulins and fractures, as happens on the Greenland Ice Sheet and temperate

mountain glaciers[50,51]. Indeed, two prior studies of $\delta^{234}U$ in subglacial waters from beneath Athabasca Glacier and the Greenland Ice Sheet do have very low values, 3–40‰ for the former[52] and 5–270‰ for the latter[32]. The Athabasca Glacier subglacial zone is flushed on seasonal timescales[52], whereas the Greenland basins examined in ref. [32] can easily have 0.1–10-yr timescales compatible with the range of values $\delta^{234}U$ observed there (Extended Data Fig. 5). In Greenland, however, these observed low $\delta^{234}U$ values come from locations where mean annual temperatures in the ablation zone are warmer than −10 °C, whereas most of the EAIS surface is an accumulation zone with mean annual temperatures falling between −30 °C and −50 °C (see ref. [53]). Occurrence of sufficient surface melting to cause large enough meltwater penetration to the ice base over current Antarctic accumulation areas would require warming of a few dozen degrees Celsius. Yet the numerical ice-sheet model[54] predicts retreat of the ice sheet from subglacial basins such as the Wilkes and Aurora basins with a much smaller thermal forcing accompanying the worst-case Representative Concentration Pathway (RCP8.5) scenario. This indicates that these marine-based regions of the ice sheet will experience grounding-line retreat due to ice–ocean interactions before an ablation zone with high surface melt and substantial water penetration to the bed develops over these regions. Therefore, our favoured interpretation for the low value of $\delta^{234}U$ around the time of MIS11 is ice-sheet retreat followed by seawater intrusion into subglacial basins located below sea level rather than a dramatic decrease in the flushing timescale not accompanied by an ice-sheet retreat.

Sample descriptions and field settings

New data presented here are from samples collected from the Pensacola Mountains and the Elephant Moraine, both within East Antarctica. A total of three samples were dated at multiple horizons (PRR16794, PRR50489 and PRR39222). These samples were provided by the Byrd Polar Rock Repository at The Ohio State University[55].

Sample PRR16794 at the Pensacola Mountains is entirely calcite and exhibits a fine-scale internal layering related to precipitate growth (Extended Data Fig. 1). The uranium content is 5 ppm. U–Th dates between the top and bottom are within uncertainty at around 200 ka but $\delta^{234}U_i$ values are resolvable from top to bottom in the range 1,875–1,990‰ (Supplementary Table 1). The $\delta^{18}O_{SMOW}$ of calcite is −9.3‰ (Extended Data Table 2). Sample PRR50489 from the Elephant Moraine consists of inter-bedded calcite and opal, exhibited in discrete layering related to precipitate growth (Extended Data Fig. 2). The $\delta^{18}O_{SMOW}$ of the calcite in this sample is −19.87‰ (Extended Data Table 2). The uranium content of calcites are <1 ppm. Opal U concentrations are in the range 10–30 ppm. U–Th dates for opals between the top and bottom of the sample span >100 thousand years in duration and exhibit $\delta^{234}U_i$ values of 1,470–2,000‰ (Extended Data Table 1).

Sample PRR39222 from the Elephant Moraine is a precipitate of black calcite. Sample PRR39222 consists of calcite sparite crystals that radiate upwards and out from nucleation surfaces. Organic material is abundant. Silicates are also present but less common. The $\delta^{18}O_{SMOW}$ of calcite from this sample is −19.45‰ (Extended Data Table 2). Bulk sample uranium concentrations are <1 ppm and $\delta^{234}U$ measured values are in the range 40–140‰ and scale with stratigraphic position in the sample (Extended Data Fig. 3, Extended Data Table 1). The U and Th composition of a calcite digested in 7N HNO_3 will represent a mixture of uranium and thorium sourced from the calcite; organics (which are abundant); and U and Th adsorbed onto silicates. Because of adsorbed thorium, we cannot determine a U–Th date and we have therefore restricted our interpretation of PRR39222 to the uranium composition alone. The uranium isotopic composition is also a mixture of the three above sources, but it can be demonstrated that the uranium sourced from the organics or adsorbed onto the surface of detrital silicates is in isotopic equilibrium with the waters that produce the calcite. A definitive test as to whether PRR39222 reliably records subglacial fluid compositions is provided by calcite analysis from sample PRR50489.

Unlike PRR39222, PRR50489 has opals that reliably record the ^{234}U ingrowth within subglacial waters. The calcite measurement from PRR50489 yields values concordant with the values for opal that lie both stratigraphically above and below (Extended Data Table 1). This strongly supports the argument that the bulk calcite digestion, despite having multiple sources of uranium, reliably records the uranium composition of the waters. The calcite from PRR50489 is very similar to PRR39222 and thus can serve as a proxy. Similarities include high Th/U; crystal morphology, of radiating sparite crystals and black colour; and nearly identical $\delta^{18}O$ and $\delta^{13}C$ values (Extended Data Table 2).

The Elephant Moraine is a supraglacial moraine—an intra-ice site of sediment and rock accumulation of a once deeply residing section of dirty basal ice. The exhumation of this basal ice section occurs as East Antarctic ice flows off the high polar plateau (>2,000 m), and into the western slopes of the Transantarctic Mountains at an elevation of 120 m below the plateau[56]. As flowing ice interacts with the underlying bedrock topography, this basal layer is transported upwards towards the ice surface[56]. Surrounding the moraine is a blue-ice area, where there is substantial loss of snow and ice to sublimation. This blue ice is just a small section of a larger sublimation belt that occurs as the thick ice of the EAIS flows eastward and is blocked by the Transantarctic Mountains[56]. The only exception to EAIS termination within such a sublimation zone is where outlet glaciers are squeezed through the major valleys cutting across the Transantarctic Mountains, such as the Taylor Glacier, which occupies Taylor Valley (see below). The occurrence of upturned ice sections from the base of the EAIS along the western flank of the Transantarctic Mountains is not uncommon. Several such sections[25,55–58], marked by both blue-ice sections bearing meteorites[58] as well as exhumed dirty basal ice layers which can contain subglacial precipitates such as those found at Elephant Moraine, Lewis Cliff[25] and in proximity to the Pensacola Mountains[55] (Fig. 1). The subglacial precipitates that form at the base of the EAIS become frozen into this debris-laden ice layer and are exhumed along with sediments and clasts. Ice ablation at the surface leaves the precipitate samples 'stranded'. The precipitates are relatively rare compared to other lithologies. It has been suggested by Taylor[59] and reviewed by Faure and Mensing[56] that the timing of supraglacial moraine inception is directly linked with the timing of thinning of the EAIS. These authors hypothesized that if East Antarctica were thicker, the ice flowing over the bedrock protrusion beneath the Elephant Moraine would have a more muted surface expression than that of a supraglacial moraine. Under this thick-ice condition, the underlying topography would induce an inflection in the ice surface but would be limited to producing a 'ramp' that may have crevasses and ice pinnacles at its crest. Under such thick-ice conditions, the EAIS dirty basal ice would not reach the surface. If the ice were to thin in response to climate, the exhumed basal ice would intersect the surface, initiating the formation of the supraglacial moraine. As such, an estimate on the timing of ice thinning can be constrained by estimates of the duration for which morainal materials have resided there, which is provided by exposure dating. Terrestrial ages exist for meteorites found within proximity (<1 km) of the moraine in blue-ice areas. The longest-exposed meteorite dates to 370 ka (ref. [60]), suggesting that the Elephant Moraine and the thinning of EAIS ice initiated no sooner than the very end of the MIS11 boundary.

The McMurdo Dry Valleys are the largest rock oasis of Antarctica, where land-terminating glaciers permit subglacial brines to emanate onto the surface or into proglacial lakes[11]. Taylor Valley, one of the McMurdo Dry Valleys, is occupied by Taylor Glacier, an outlet glacier of the EAIS, and is one of the many narrow mountain passes through which the EAIS extrudes as it flows from the high polar plateau towards the coast. Subglacial discharge reaches the surface at the snout of Taylor Glacier. There hypersaline fluids emanate seasonally in what is referred to as 'Blood Falls' owing to the iron oxides that form upon oxidation

of soluble iron[10,12,61]. Subglacial discharge of brines is also detected, geochemically at depth within the proglacial lake (Lake Bonney) that abuts Taylor Glacier[8,62]. Surveys using airborne transient electromagnetics to image resistivity identify high-solute liquids connecting Lake Bonney to a subglacial region that extends up-glacier for kilometres until increased ice thickness prevents further detection[11]. It has been speculated that these fluids extend the length of Taylor Glacier back to the EAIS[11]. The δ^{234}U composition of subglacial discharge in Taylor Valley is in the range 3,500–5,000‰ (Fig. 1, 3)[8,10]. Similarly ^{234}U-enriched waters are observed in groundwater-fed lakes in Wright Valley, immediately to the north of Taylor Valley[8], suggesting that such subglacial discharge has a role in the formation and composition of these lakes as well. Such an observation suggests a shared source for Wright Valley and Taylor Valley fluids and supports speculation that all McMurdo Dry Valleys fluids are sourced from beneath the EAIS. This fuels further speculation that such fluids occur throughout the EAIS but are more readily observed in locations where glaciers terminate on land. Within the McMurdo Dry Valleys lakes, Holocene age carbonates record δ^{234}U compositions similar to modern waters[9]. Similar lakes are theorized to occupy Taylor Valley at each interglacial period over the past 350 kyr or so[9]. As discussed in the main text, the δ^{234}U composition of these past carbonates reflects an origination from a ^{234}U-enriched subglacial reservoir and that this reservoir increases in ^{234}U with time, suggesting a coevolution with fluids within the Wilkes Basin. In addition to the age constraints provided by the apparent ^{234}U ingrowth record (Fig. 3), noble gas measurements from the deep waters of the modern Lake Bonney fed by subglacial discharge[11] provide additional age constraints. Excess in both ^{4}He and ^{40}Ar up to 200× atmospheric values point to fluid isolation from the atmosphere and contact with rock on durations that exceed 200 kyr (refs. [29,30]). This is a minimum estimate, as any dilution by surface waters that exist in the shallow waters of Lake Bonney would yield an apparently younger date. Although these authors suggest that such isolation occurred in situ within Lake Bonney, a compelling documentation for glacial advance and retreat on glacial–interglacial timescales[9,63,64] that implies that Taylor Glacier at times occupied the extent of Taylor Valley and reached the Ross Sea suggests that Lake Bonney is an ephemeral feature. In short, these waters did not reside in Lake Bonney for 200 kyr because Lake Bonney did not exist at that time and was filled by ice during the documented expansions of Taylor Glacier. The detection of subglacial discharge beneath Taylor Glacier provides a solution[11]—the long-term isolation of fluids occurred not in Lake Bonney but beneath the EAIS before their passage beneath Taylor Glacier and into the proglacial Lake Bonney.

Data availability

All data used are included within the Extended Data Tables 1–4 and Extended Data Figs. 1–5 and uploaded to https://doi.org/10.26022/IEDA/111548.

Code availability

Any codes used are available upon request.

42. Condon, D. J., McLean, N., Noble, S. R. & Bowring, S. A. Isotopic composition (^{238}U/^{235}U) of some commonly used uranium reference materials. *Geochim. Cosmochim. Acta* **74**, 7127–7143 (2010).
43. Hamelin, B., Bard, E., Zindler, A. & Fairbanks, R. G. ^{234}U/^{238}U mass spectrometry of corals: how accurate is the U–Th age of the last interglacial period? *Earth Planet. Sci. Lett.* **106**, 169–180 (1991).
44. Cheng, H. et al. Improvements in ^{230}Th dating, ^{230}Th and ^{234}U half-life values, and U–Th isotopic measurements by multi-collector inductively coupled plasma mass spectrometry. *Earth Planet. Sci. Lett.* **371/372**, 82–91 (2013).
45. Andersen, M. B., Erel, Y. & Bourdon, B. Experimental evidence for ^{234}U–^{238}U fractionation during granite weathering with implications for ^{234}U/^{238}U in natural waters. *Geochim. Cosmochim. Acta* **73**, 4124–4141 (2009).
46. Prentice, M. L. & Matthews, R. K. Tertiary ice sheet dynamics: the snow gun hypothesis. *J. Geophys. Res. Solid Earth* **96**, 6811–6827 (1991).
47. Christoffersen, P., Bougamont, M., Carter, S. P., Fricker, H. A. & Tulaczyk, S. Significant groundwater contribution to Antarctic ice streams hydrologic budget. *Geophys. Res. Lett.* **41**, 2003–2010 (2014).
48. Dowdeswell, J. A. & Siegert, M. J. Ice-sheet numerical modeling and marine geophysical measurements of glacier-derived sedimentation on the Eurasian Arctic continental margins. *Geol. Soc. Am. Bull.* **111**, 1080–1097 (1999).
49. Tulaczyk, S., Kamb, B. & Engelhardt, H. F. Estimates of effective stress beneath a modern West Antarctic ice stream from till preconsolidation and void ratio. *Boreas* **30**, 101–114 (2001).
50. Howat, I. M., Joughin, I., Tulaczyk, S. & Gogineni, S. Rapid retreat and acceleration of Helheim Glacier, east Greenland. *Geophys. Res. Lett.* **32**, L22502 (2005).
51. Howat, I. M., Tulaczyk, S., Waddington, E. & Björnsson, H. Dynamic controls on glacier basal motion inferred from surface ice motion. *J. Geophys. Res. Earth Surf.* **113**, F03015 (2008).
52. Arendt, C. A., Aciego, S. M., Sims, K. W. W. & Aarons, S. M. Seasonal progression of uranium series isotopes in subglacial meltwater: implications for subglacial storage time. *Chem. Geol.* **467**, 42–52 (2017).
53. Bréant, C., Martinerie, P., Orsi, A., Arnaud, L. & Landais, A. Modelling firn thickness evolution during the last deglaciation: constraints on sensitivity to temperature and impurities. *Clim. Past* **13**, 833–853 (2017).
54. Golledge, N. R. et al. The multi-millennial Antarctic commitment to future sea-level rise. *Nature* **526**, 421–425 (2015).
55. The Polar Rock Repository. *Archive of information about geological samples available for research from the Ohio State University Byrd Polar and Climate Research Center (BPCRC) Polar Rock Repository* https://data.nodc.noaa.gov/cgi-bin/iso?id=gov.noaa.ngdc.mgg.geology:archived-data_BPCRC-polar-rock-repository (NOAA National Centers for Environmental Information, 2019).
56. Faure, G. & Mensing, T. M. *The Transantarctic Mountains: Rocks, Ice, Meteorites And Water* (Springer Science & Business Media, 2010).
57. Faure, G. & Taylor, K. S. The geology and origin of the Elephant Moraine on the East Antarctic Ice Sheet. *Antarct. J. US* **20**, 11 (1985).
58. Cassidy, W., Harvey, R., Schutt, J., Delisle, G. & Yanai, K. The meteorite collection sites of Antarctica. *Meteoritics* **27**, 490–525 (1992).
59. Taylor, K. S. *Lithologies and Distribution of Clasts in the Elephant Moraine, Allan Hills South Victoria Land, Antarctica*. MSc thesis, Kent State Univ. (1986).
60. Nishiizumi, K., Elmore, D. & Kubik, P. W. Update on terrestrial ages of Antarctic meteorites. *Earth Planet. Sci. Lett.* **93**, 299–313 (1989).
61. Lyons, W. B. et al. Halogen geochemistry of the McMurdo Dry Valleys lakes, Antarctica: clues to the origin of solutes and lake evolution. *Geochim. Cosmochim. Acta* **69**, 305–323 (2005).
62. Lyons, W. B. et al. Strontium isotopic signatures of the streams and lakes of Taylor Valley, Southern Victoria Land, Antarctica: chemical weathering in a polar climate. *Aquat. Geochem.* **8**, 75–95 (2002).
63. Brook, E. J. et al. Chronology of Taylor Glacier advances in Arena Valley, Antarctica, using in situ cosmogenic ^{3}He and ^{10}Be. *Quat. Res.* **39**, 11–23 (1993).
64. Bockheim, J. G., Prentice, M. L. & McLeod, M. Distribution of glacial deposits, soils, and permafrost in Taylor Valley, Antarctica. *Arct. Antarct. Alp. Res.* **40**, 279–286 (2008).

Acknowledgements We thank J. Schutt, G. Faure and D. Schmidt for their sample collection at the Elephant Moraine and A. Grunow and the Byrd Polar Rock Repository for providing samples with a 'PRR' prefix. We also thank J. Paces, S. Hemming and T. Rasbury for their input. This research was funded by NSF 1644171 to T.B. and S.T.

Author contributions T.B. wrote the manuscript, led this study and developed the U-series methods. G.H.E. performed model simulations, tracer calibration and U-series data reduction. S.T. interpreted data and performed modelling. M.S. prepared samples and performed clean laboratory work. G.P. performed clean laboratory work and tracer calibration. N.McL. did the maximum likelihood model construction. B.H. interpreted data. J.C.Z. performed the oxygen isotopic analyses. B.C. did the SEM imaging. J.T.B. prepared samples and performed clean laboratory work.

Competing interests The authors declare no competing interests.

Additional information

Supplementary information is available for this paper at https://doi.org/10.1038/s41586-020-2484-5.

Correspondence and requests for materials should be addressed to T.B.

Peer review information *Nature* thanks Carli Arendt and the other, anonymous, reviewer(s) for their contribution to the peer review of this work.

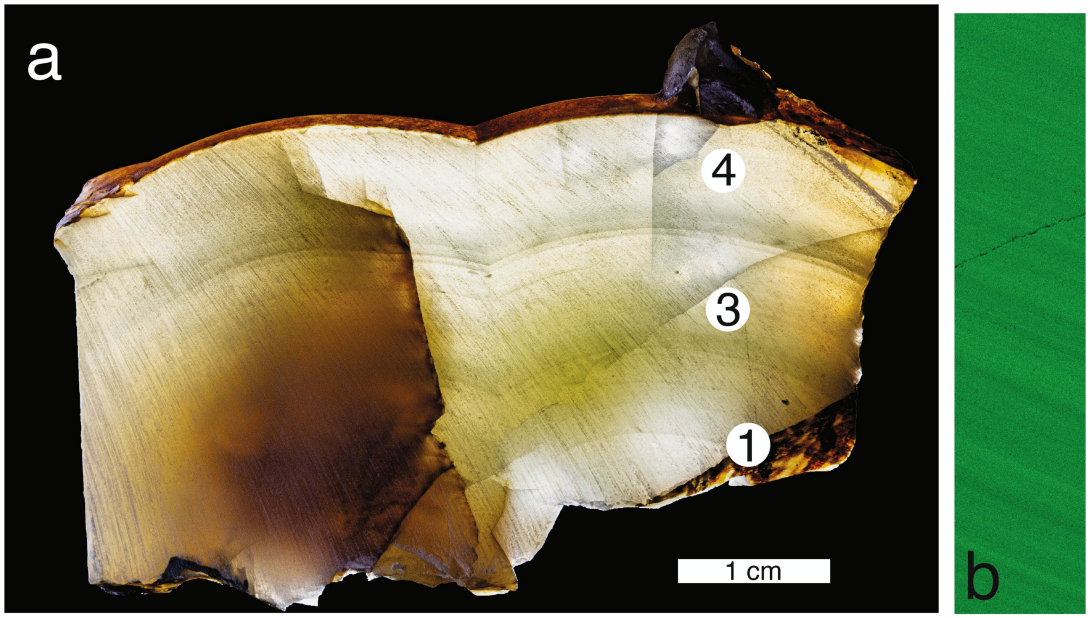

Extended Data Fig. 1 | Images of sample PRR16794. a, **b**, Sample shown in visible light (with location of dated horizons corresponding to data reported in Extended Data Table 1) (**a**) and the scanning electron microscope (SEM)/ energy-dispersive X-ray spectroscopy (EDS) compositional map showing variations in manganese (green for high Mn, black for low Mn) (**b**).

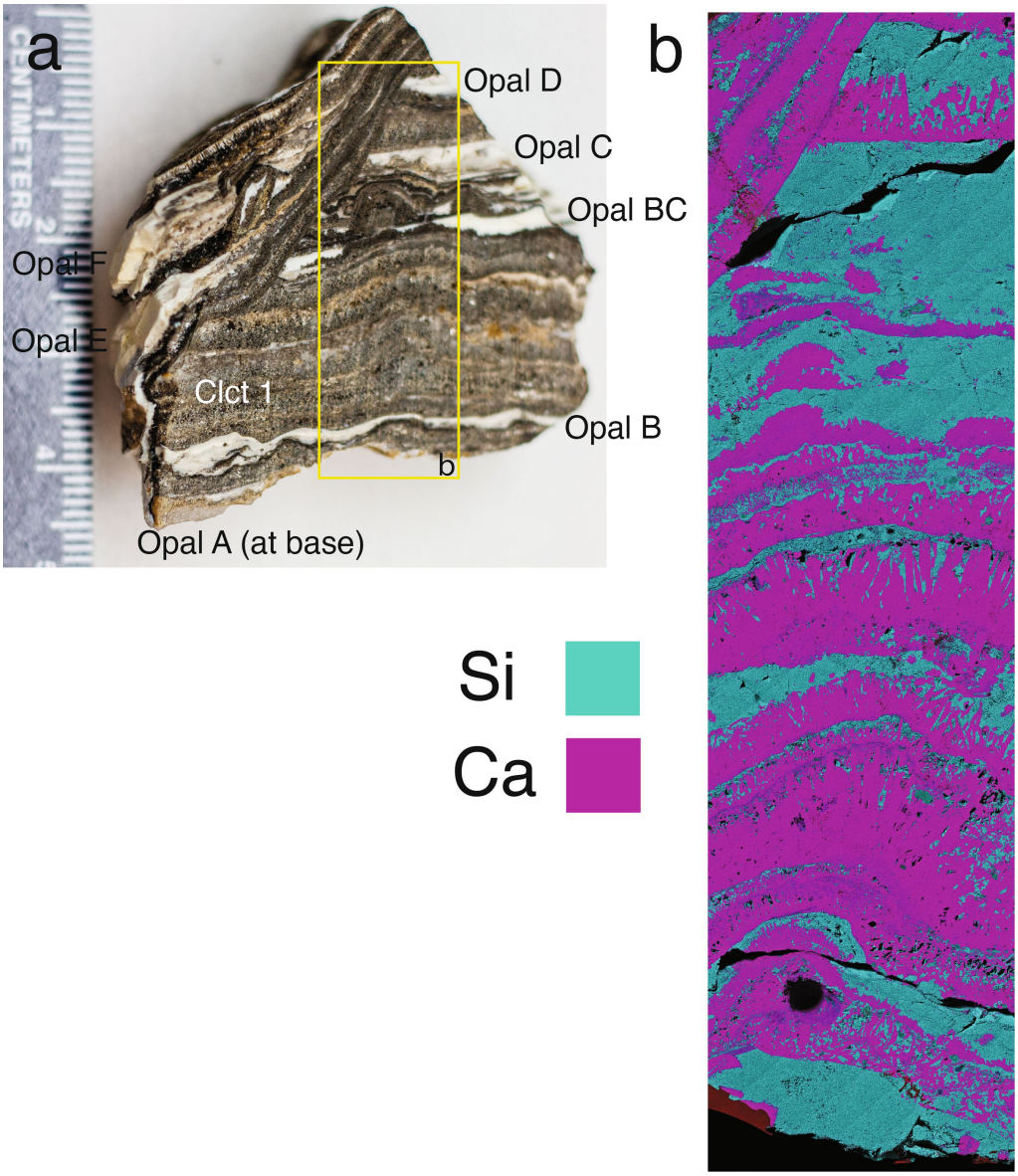

Extended Data Fig. 2 | Images of sample PRR50489. a, **b**, Sample shown in visible light (with location of dated horizons corresponding to data reported in Extended Data Table 1) (**a**) and the SEM/EDS compositional map showing Ca and Si (**b**). The sample exhibits an angular unconformity, indicating that the sample physically moved beneath the ice before accumulation began again. Clct, calcite.

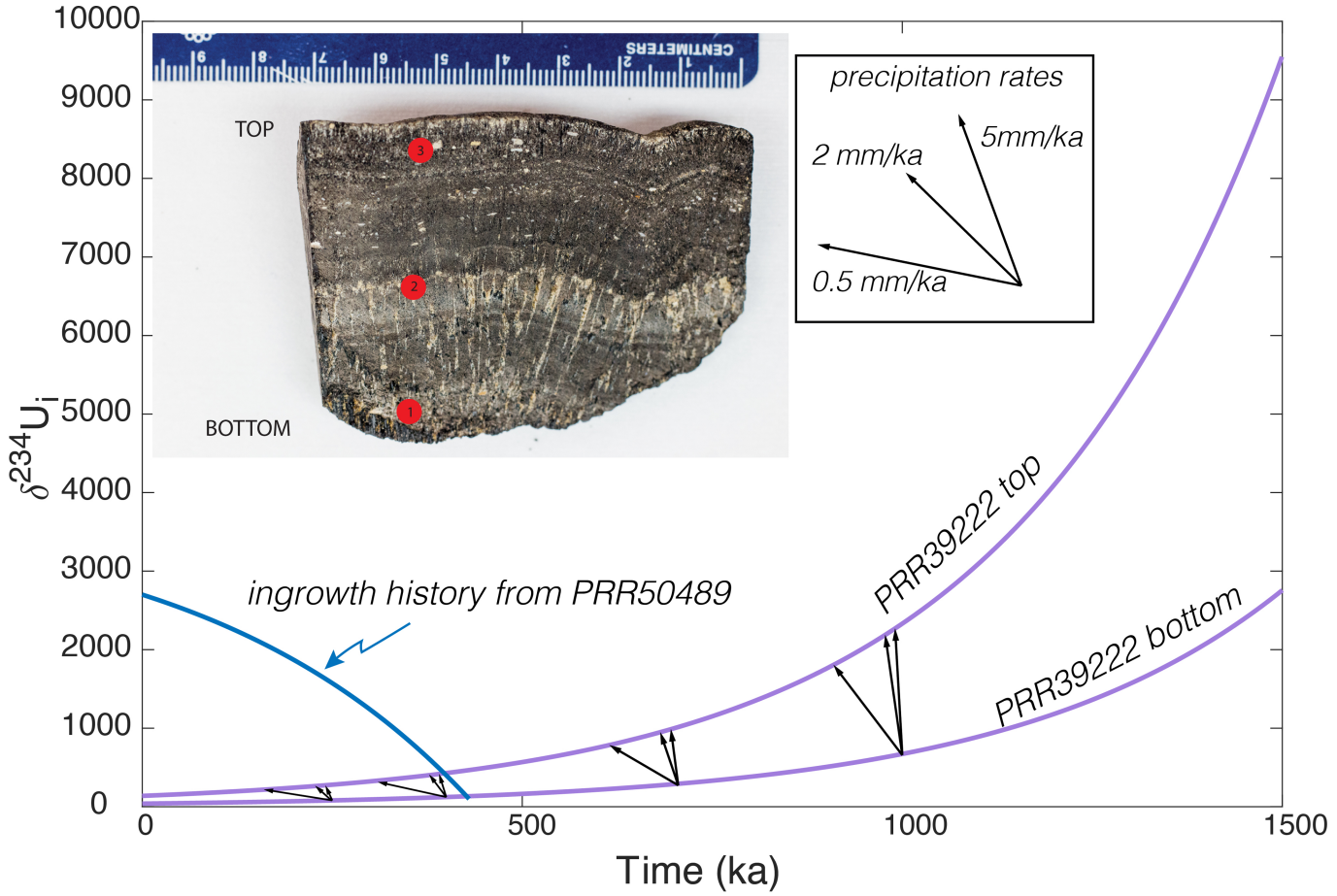

Extended Data Fig. 3 | Model constraints on ^{234}U ingrowth history of PRR39222. The inset photograph shows sample PRR39222 under visible light with the location of $\delta^{234}U$ measurements marked. The main plot shows the measured $\delta^{234}U$ for PRR39222 at three horizons, revealing an increasing $\delta^{234}U$ from top to bottom (Extended Data Table 1). Because of the high thorium (Th) contents, we cannot define a formation age and thus cannot identify a reliable $\delta^{234}U_i$. The purple curves in Fig. 3 represent the possible $\delta^{234}U_i$ values for the top (higher $\delta^{234}U$) and bottom (lower $\delta^{234}U$) for any formation time. What we do not know is the absolute time at which this sample formed or the duration it formed over. However, we do know that: (1) the $\delta^{234}U_i$ for the top and bottom of the sample must lie on these purple lines; (2) the sample must be younger than 1,500 kyr given that the measured $\delta^{234}U$ is not in secular equilibrium. In addition to these known conditions, we can assume that the calcite in PRR39222 probably formed very rapidly as indicated by: (1) morphology, specifically radiating clusters of blade-like sparite; (2) lack of unconformities; (3) shared $\delta^{18}O$ and $\delta^{13}C$ composition with rapidly forming calcite from PRR50489, which is constrained by geochronology. Data from the literature as well as the geochronologic constraints presented in Extended Data Table 1 provide limits on the rate of sub-ice calcite formation (0.5 mm kyr^{-1} is shallow and 5 mm kyr^{-1} is steep). Given a known sample dimension of 4.5 cm, any assumed precipitation rate translates to a time duration for sample formation of 10–90 kyr. Assuming these durations, along with the requirement that the bottom and top of the sample intersects the purple curves in Fig. 3, permits us to define possible $\delta^{234}U_i$ ingrowth histories (black arrows in Fig. 3). The rate of modelled ^{234}U accumulation as recorded by PRR39222 is strongly controlled by assumed formation age with only a narrow time range yielding ^{234}U ingrowth histories consistent with the other Wilkes Basin fluid histories. For example, if the sample were to have formed at 1,000 ka, we predict a change in $\delta^{234}U_i$ of about 300% from the top to the bottom of this sample. Such rapid ingrowth histories result in $\delta^{234}U$ compositions that would result in $\delta^{234}U$ compositions that far exceeds anything observed in Antarctica (>6,000‰). If, however, the sample were to have formed at about 400 ka, the projected ingrowth histories would match both model projections and measured data for the Wilkes Basin. Only scenarios that place PRR39222 formation at roughly <500 ka yield projected ingrowth histories consistent with the blue curve. In addition to the above analysis, the occurrence of low $\delta^{234}U$ (<500‰) in subglacial fluids is apparently rare, having been identified in this region only in samples older than about 300 ka. Collectively, this suggests that the ^{234}U ingrowth history recorded by PRR39222 is at least consistent with formation at about 400 ka.

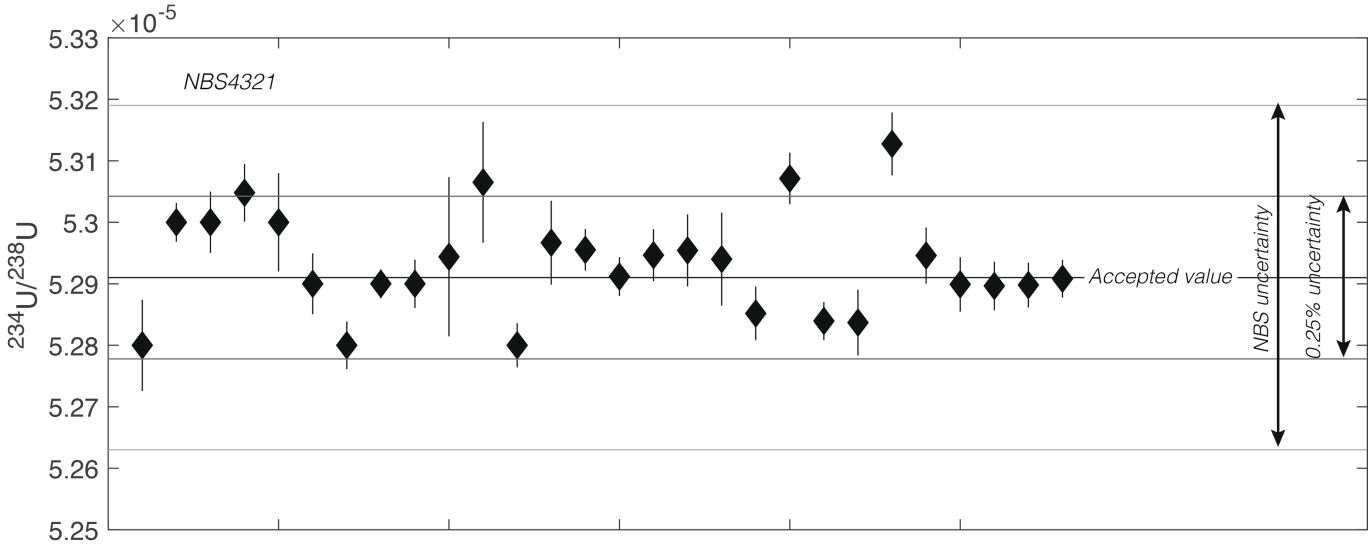

Extended Data Fig. 4 | Long-term results of measurements of NBS 4321 ($5.2919 \times 10^{-5} \pm 0.013 \times 10^{-5}$ (0.25%)) at UCSC using an IsotopX X62, TIMS. All uncertainties are absolute 2σ.

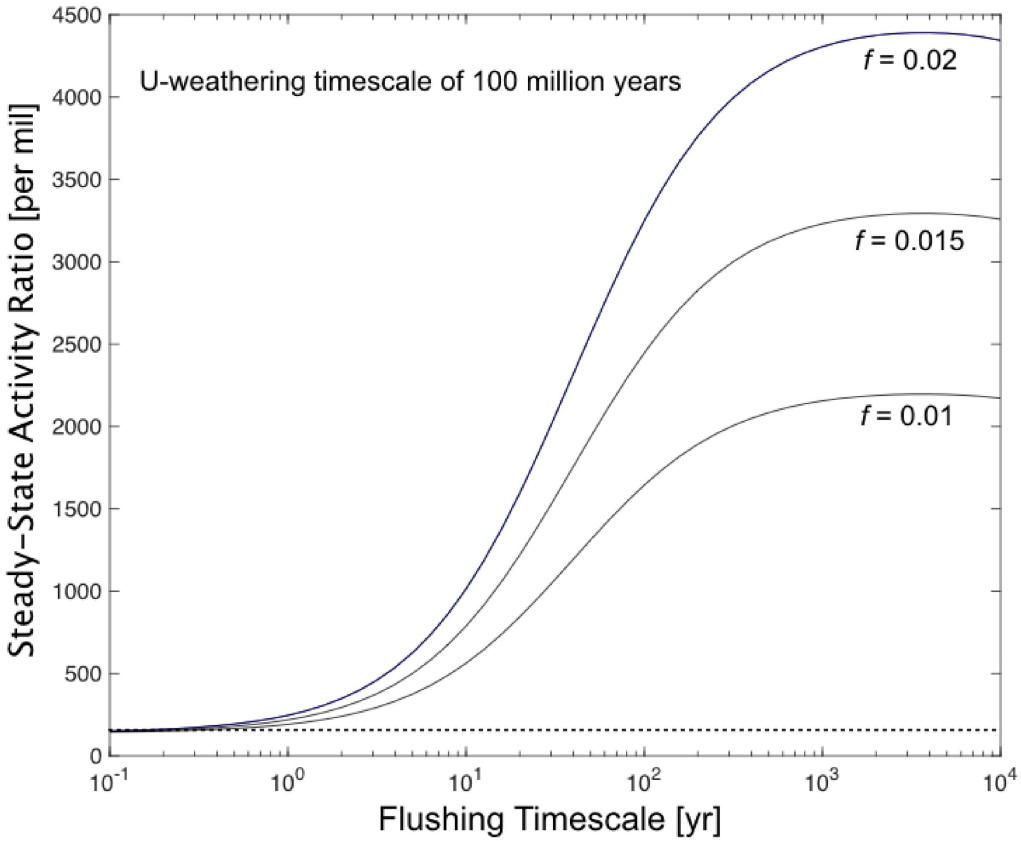

Extended Data Fig. 5 | Steady-state activity ratio of ^{234}U and ^{238}U as a function of the flushing timescale for three different values of the ^{234}U ejection factor. The dotted line shows the assumed level of $\delta^{234}U$ in meltwater. The assumed weathering timescale is 100 million years.

Extended Data Table 1 | U-series data from EAIS precipitates

sample name	mineralogy	Th (ppm)	U (ppm)	232Th/238U	2s unc	[230Th/232Th]	2s unc	[230Th/234U]	2s unc	[234U/238U]	2s unc	U-Th age (ka)	2s unc	[234U/238U]i	2s unc
PRR50489_Op_F2	opal	0.04	29.92	0.0012	0.0000	4952.031	0.009	0.8402	0.0198	2.2983	0.0016	154.69	3.61	3.01	0.07
PRR50489_OpE_1	opal	0.20	28.39	0.0071	0.0001	866.675	0.002	0.8512	0.0158	2.2934	0.0033	158.60	3.73	3.02	0.07
PRR50489_OpD_1	opal	0.41	11.57	0.0366	0.0007	176.415	0.003	0.8760	0.0162	2.3441	0.0324	167.08	5.08	3.15	0.11
PRR50489_OpC_3	opal	0.24	4.32	0.0559	0.0010	112.840	0.009	0.9401	0.0198	2.1313	0.0025	197.30	5.31	2.98	0.08
PRR50489_OpBC_1	opal	0.73	15.20	0.0490	0.0009	128.520	0.006	0.9538	0.0182	2.1229	0.0153	196.11	6.24	2.98	0.10
PRR50489_OpB_1	opal	1.29	11.99	0.1100	0.0020	55.220	0.003	0.9712	0.0180	1.9895	0.0031	217.01	5.06	2.83	0.07
PRR50489_OpB_2	opal	0.08	2.11	0.0399	0.0007	153.970	0.010	0.9737	0.0204	2.0056	0.0061	217.90	5.59	2.86	0.07
PRR50489_OpA_3	opal	0.22	5.16	0.0432	0.0008	124.740	0.007	1.0098	0.0199	1.6954	0.0332	256.42	12.48	2.43	0.13
PRR50489_OpA_2	opal	0.43	14.20	0.0313	0.0006	186.300	0.004	1.0020	0.0188	1.8523	0.0023	241.41	5.70	2.68	0.06
PRR50489_OpA_4	opal	0.16	4.61	0.0360	0.0007	150.014	0.014	1.0187	0.0232	1.6861	0.0224	264.46	8.75	2.45	0.09
PRR50489_Clct_1	calcite	2.05	0.60	3.4901	0.0639	1.810	0.032	1.0654	0.0396	1.8853	0.0058	-	-	-	-
PRR50489_Clct_1.2	calcite	-	0.34	-	-	-	-	-	-	1.9817	0.0394	-	-	-	-
PRR16794_1_2	calcite	1.13	5.24	0.2206	0.0040	27.820	0.004	0.9490	0.0176	2.0563	0.0062	203.39	4.84	2.88	0.07
PRR16794_1_3	calcite	1.12	5.22	0.2199	0.0040	27.713	0.006	0.9408	0.0181	2.0600	0.0032	199.23	4.71	2.86	0.07
PRR16794_3_2	calcite	1.00	7.14	0.1431	0.0027	44.286	0.006	0.9447	0.0186	2.1339	0.0021	199.49	4.73	2.99	0.07
PRR16794_4_2	calcite	1.63	8.25	0.2029	0.0044	31.202	0.014	0.9507	0.0246	2.1177	0.0022	202.80	5.28	2.98	0.08
PRR39222_1_1	calcite	-	0.38	-	-	-	-	-	-	1.0419	0.0099	-	-	-	-
PRR39222_2_1	calcite	0.41	0.22	1.8834	0.0344	1.869	0.032	1.0548	0.0386	1.0611	0.0059	-	-	-	-
PRR39222_2_2	calcite	0.86	0.34	2.5517	0.0509	2.054	0.017	1.5463	0.0407	1.0781	0.0034	-	-	-	-
PRR39222_3_1	calcite	2.78	0.47	6.1161	0.1118	0.632	0.017	1.0845	0.0274	1.1342	0.0064	-	-	-	-
PRR39222_3_2	calcite	2.69	0.45	6.1906	0.1155	0.615	0.016	1.0631	0.0260	1.1387	0.0164	-	-	-	-

All uncertainties are absolute 2σ ('2s unc'). Age uncertainties do not include decay constant uncertainties.

Extended Data Table 2 | Oxygen and carbon isotopic data from EAIS precipitates

Sample ID	Weight (mg)	$CaCO_3$ (%)	$\delta^{13}C_{VPDB}$ (‰)	$\delta^{18}O_{VPDB}$ (‰)	$\delta^{18}O_{SMOW}$ (‰)
PRR 50489_1	0.122	87.70	-22.84	-48.84	-19.87
PRR 50488_1	0.081	107.41	-23.20	-45.15	-16.03
PRR 39222_1	0.131	106.87	-23.17	-48.44	-19.45
PRR 16794_1	0.098	112.24	-21.20	-38.70	-9.32

Data were measured at the University of California, Santa Cruz Stable Isotope Laboratory on the Kiel IV and Thermo Mat253. VPDB, the Vienna Pee-Dee belemnite standard; SMOW, standard mean ocean water.

Extended Data Table 3 | U-series standard data collected at UCSC and accepted ages

sample name	19ACAG8a_4_1_0.5cm depth	19ACAG8a_1_2cm depth	9ACAG8a_2_7cm_depth	OP_SE_1	Reef5e_3_2	Reef5e_3_3	Reef5e_4_3	Reef_5e_6	Reef5e_7
U(ng)	5296.54	3358.79	5960.89	209.87	779.33	772.48	1000.91	210.10	814.94
Th(ng)	13.10	7.73	5.73	3.29	0.07	0.06	0.13	0.06	0.19
Th (ppm)	0.13	0.11	0.06	0.62	0.00	0.00	0.00	0.00	0.00
U (ppm)	53.61	49.11	57.59	39.60	3.88	3.24	3.96	4.00	3.94
232Th/238U	0.00	0.00	0.00	0.02	0.00	0.00	0.00	0.00	0.00
2s unc	0.00	0.00	0.00	0.00	0.00	0.00	0.00	0.00	0.00
[230Th/232Th]	889.8230	1005.4207	2805.9494	197.5654	28609.1260	29970.5025	18857.7597	9204.0819	10360.5269
2s unc	0.0024	0.0082	0.0121	0.0035	0.0131	0.0082	0.0080	0.0245	0.0093
[230Th/234U]	0.1504	0.1577	0.1864	1.0091	0.7021	0.7023	0.6881	0.7205	0.7026
2s unc	0.0028	0.0032	0.0042	0.0187	0.0173	0.0146	0.0140	0.0229	0.0152
[234U/238U]	4.7751	4.7839	4.7184	1.0003	1.1368	1.1439	1.1471	1.1449	1.1433
2s unc	0.0165	0.0021	0.0025	0.0013	0.0024	0.0014	0.0017	0.0029	0.0027
[234U/238U]initial	4.9652	4.9846	4.9555	1.0021	1.1959	1.2060	1.2077	1.2111	1.2052
U-Th age (ka)	17.41	18.31	21.91	>1500	127.22	127.09	122.38	133.26	127.20
2s unc	0.44	0.44	0.57	17.14	3.06	2.97	4.12	5.07	3.18
Accepted age:	depth dependent (>10cm depth = 21.9 ka; 1-6 cm = 17.8-19.3 ka)			>1500	122-132.4 ka	122-132.4 ka	122-132.4 ka	122-132.4 ka	122-132.4 ka
reference	Frisia et al., 2017	Frisia et al., 2017	Frisia et al., 2017	NA	Hamelin et al., 1991	Hamelin et al., 1991	Hamelin et al., 1991	Hamelin et al., 1991	Hamelin et al., 1991

All uncertainties are absolute 2σ. Age uncertainties do not include decay constant uncertainties. Data are from Frisia et al.[24] and Hamelin et al.[43].

Extended Data Table 4 | Legacy U-series recalculated using refined decay constants 2σ

sample	age*	2s	d234U*	2s	publication
74-29	2.01	0.24	2287.9	60	Hendy et al., 1979
74-30	4.10	0.86	2311.5	200	Hendy et al., 1979
74-56	1.78	0.28	2286.4	80	Hendy et al., 1979
74-57	1.83	0.24	2606.9	80	Hendy et al., 1979
74-58	9.37	1.20	2877.6	240	Hendy et al., 1979
74-90	5.20	0.38	3126.8	240	Hendy et al., 1979
76-4	71.89	2.80	2494.0	60	Hendy et al., 1979
76-8	75.84	5.20	2078.1	40	Hendy et al., 1979
75-8	78.41	5.60	2391.3	100	Hendy et al., 1979
75-26	89.16	4.80	2068.1	20	Hendy et al., 1979
75-29	86.96	5.20	2131.6	40	Hendy et al., 1979
76-7	91.41	4.00	2274.5	40	Hendy et al., 1979
76-6	89.56	2.80	2724.0	60	Hendy et al., 1979
76-14	73.91	3.20	2299.8	80	Hendy et al., 1979
75-22	89.30	9.00	2824.5	100	Hendy et al., 1979
74-36	94.63	3.20	2165.3	40	Hendy et al., 1979
75-11	97.29	3.40	3111.6	320	Hendy et al., 1979
75-18	99.38	6.00	2273.5	60	Hendy et al., 1979
76-9	120.21	6.00	2439.1	60	Hendy et al., 1979
76-5	117.66	12.00	2865.6	80	Hendy et al., 1979
75-I	127.89	10.00	3092.4	60	Hendy et al., 1979
74-24	210.49	20.00	1253.8	40	Hendy et al., 1979
74- 19	217.31	20.00	1259.8	20	Hendy et al., 1979
74-20	203.49	20.00	1353.0	20	Hendy et al., 1979
74-23	193.20	16.00	1468.8	20	Hendy et al., 1979
75-13	200.50	20.00	1306.6	60	Hendy et al., 1979
15-27	214.45	20.00	1960.7	60	Hendy et al., 1979
76-1	209.83	30.00	2673.1	160	Hendy et al., 1979
76- 17	224.12	20.00	113.2	10	Hendy et al., 1979
75-16	286.35	100.00	570.4	40	Hendy et al., 1979
76-11	302.88	40.00	1352.4	90	Hendy et al., 1979
76-10	314.88	100.00	473.0	20	Hendy et al., 1979
1	24.56	0.10	4040.3	65	Fitzpatrick et al., 1990
2a	21.51	0.10	3190.2	58	Fitzpatrick et al., 1990
2b	34.47	0.71	2260.2	51	Fitzpatrick et al., 1990
2d	9.97	0.10	2240.1	66	Fitzpatrick et al., 1990
2d	37.73	1.06	2930.3	97	Fitzpatrick et al., 1990

Age uncertainties do not include decay constant uncertainties. Data are from Hendy et al.[9] and Fitzpatrick et al.[25].